J. Appl. Comput. Mech., xx(x) (2026) 1-15
DOI: 10.22055/jacm.2026.48900.5585

ISSN: 2383-4536
jacm.scu.ac.ir

Shahid Chamran University of Ahvaz

Journal of Applied and Computational Mechanics

Research Paper

Vibration and Energy Optimization in Offshore Wind Towers via Time-Delayed Nonlinear Integral Positive Position Feedback Control

T.S. Amer[1], M.K. Abohamer[2], T.A. Bahnasy[2], I.S. Hamada[1], A.M. Farag[1]

[1] Department of Mathematics, Faculty of Science, Tanta University, Tanta 31527, Egypt,
tarek.saleh@science.tanta.edu.eg (T.S.A.); ebrahim_63821_pg@science.tanta.edu.eg (I.S.H); afaf.hussien@science.tanta.edu.eg (A.M.F.)

[2] Department of Engineering Physics and Mathematics, Faculty of Engineering, Tanta University, Tanta 31734, Egypt,
mohamed.abohamer@f-eng.tanta.edu.eg (M.K.A.); taher.bahnasy@f-eng.tanta.edu.eg (T.A.B.)

Received November 11 2025; Revised April 05 2026; Accepted for publication May 07 2026.
✉ Corresponding author: M.K. Abohamer (mohamed.abohamer@f-eng.tanta.edu.eg)

Abstract. The main scope of this research is to analyze the control of energy transmission and oscillation effectiveness in mathematical applications, specifically represented by the first bending mode of offshore wind turbine towers, using a superposition of excitations. Due to the generation of overlapping multi-resonance obstacles and ignorance of feedback delays in most conventional passive and active devices, the time-delayed nonlinear integral positive position feedback (TD-NIPPF) controller is employed to prevent the turbine structure from harmful oscillations and regulate energy transmission of the wind turbine, particularly at resonance states. The model's governing equation (GE) has been approximated to 2nd order using the multiple-scales approach (MSA), and the approximated outcomes are compatible with those acquired numerically through the 4th order Runge-Kutta method (RK-4). Moreover, modulation equations are extracted through the solvability conditions after inserting the resonant states. Additionally, Wolfram Mathematica and MATLAB are implemented to graphically construct the frequency response curves and time response diagrams of the acquired solutions in the presence and without the TD-NIPPF controller. Additionally, the parameter effects are graphically illustrated for the most significant factors on the wind structure. Bifurcation diagrams, Largest Lyapunov exponent (LLE), Poincaré maps, and phase portraits are plotted to illustrate the system's various dynamic behaviors. Lastly, stability examinations and steady-state solutions will be discussed via resonance curves. Moreover, the numerical findings demonstrated that the TD-NIPPF strategy effectively diminished tower distortion response across a wide spectrum of operating conditions, while ensuring stability within time delays and surpassing standard linear control setups in multi-excitation resonance scenarios.

Keywords: Offshore wind turbine structure; Time-delayed nonlinear integral positive position feedback control; Stability; Bifurcation analysis; Large Lyapunov exponent.

1. Introduction

In recent decades, renewable energy has significantly contributed to advancing sustainable development, promoting cost-effectiveness, and driving scientific progress toward a cleaner, brighter future. As global energy demand continues to rise, there is a growing need to explore alternative methods of energy generation, supporting the global transition toward cleaner energy solutions. Among the various renewable sources, wind energy has emerged as a leading option, mainly due to its declining costs. Further, wind turbines are more than just a clean energy source [1, 2]. Scientists have helped cut back on dirty carbon, speed up installations, steady towers, and gain new economic insights into the planet. Further, the literature on integrating structural control with offshore wind turbines is provided. The researchers installed a vibration isolation device at the top of wind turbine towers to measure its effectiveness on wind-induced and seismic structural responses. They observed a significant reduction in response parameters, which provided a viable design for wind turbines in seismically active regions [3]. Dagli et al. [4] employed two different strategies for observing the dynamic response of an offshore wind turbine system to seismic and environmental forces. The outcomes displayed high consistency with each other, suggesting that Rayleigh's method serves as an efficient tool for initial structural examinations. The structural difficulties associated with offshore wind turbine foundations for both fixed and floating wind turbines are reviewed. It also developed further research to enhance design codes, computerized modeling, and field validation [5]. Fang et al. [6] examined key components of designing wind-turbine towers, how they're built, the loads they encounter from wind, waves, and earthquakes, and the types of foundations used on land and at sea. It also suggests using new materials and hybrid designs to make the towers more efficient and less expensive.

The examination of wind and wave loads on offshore turbines was conducted by Liu et al. [7], and it was found that aerodynamic damping is key to reducing vibrations and wear on the tower, making it central to upcoming turbine designs. Fitzgerald et al. [8]

Published online: May 13 2026

investigated how active tuned mass dampers enhance wind turbine tower durability and mitigate wind load-induced vibrations. The behavior of a nonlinear cable-stayed beam under a time-delay feedback controller was investigated. The obtained results by Peng et al. [9] revealed that choosing optimal settings for displacement- or acceleration-feedback control considerably dampened resonance—doing a better job than velocity-based control. The authors then tested the dynamics, stability, and energy transfer of an offshore turbine tower when subjected to multiple external loads, applying both proportional-derivative (PD) and nonlinear PD control strategies. To illustrate the impact of control parameters, the authors presented frequency-response curves, Poincare maps and bifurcation diagrams at some parameters through applying various perturbation techniques, the results revealed that both controllers not only significantly suppressed high- amplitude wind oscillations but also facilitated efficient energy redistribution from uncontrolled to controlled states, with reasonable agreement between analytical predictions and numerical validations, underscoring its potential for enhancing structural stability under resonant cases [10, 11].

The NIPPF controller was implemented by Abualnaja et al. [12] to study the nonlinear vibration regulation of a van der Pol-Duffing oscillator that was driven by external and parametric excitations. Multiple-scales approach [13] and frequency-response plots showed that the controller slashed vibration by an astounding 99.995%. The same study also reviewed wind-turbine vibration controls, sorting them into six basic types. It weighed each method's pros, cons, and maturity level, and stressed the need for more real-world tests and scaling work before these solutions can be rolled out widely [14, 15]. With an emphasis on evaluating how time delay affects stability and the effectiveness of vibration suppression, Kandil and El-Ganaini [16] investigated the application of a time-delayed positive position feedback (PPF) control approach to mitigate nonlinear oscillations in rotating blades. As long as the time delay stays below a predetermined critical limit, analytical and numerical findings verify that the controller has significantly mitigated vibration. To modulate high amplitudes in a Duffing oscillator under resonant conditions [17], a negative velocity feedback (NVF) controller was applied, incorporating a time delay. The approximate analytical solutions and stability analysis were evaluated through the time scales perturbation technique, which demonstrated that time delay and optimized feedback parameters greatly suppress oscillations, as indicated by numerical validation. Hamed and Kandil [18] analyzed the effect of time-delayed nonlinear saturation control (NSC) on the oscillatory motion and energy transmission of rotating blades, adopting the Lyapunov linearization approach, which enabled them to optimize the produced oscillations. Lackner and Rotea [19] explored how passive control systems, like tuned mass dampers (TMDs), can stabilize offshore wind turbines by reducing structural vibrations. In addition, they developed a simulation tool to evaluate TMDs on various turbine foundations, indicating that TMDs operated efficiently for floating barges but had a limited impact on fixed monopiles due to the effects of wave forces. Moreover, the implementation of an inverted pendulum TMD and an active TMD through offshore wind turbines enabled the authors to eliminate undesired tower oscillations induced by wind and wave forces. Simulations demonstrated that active TMD was more effective than passive dampers in lowering structural response without adding damper mass [20, 21]. On top of that, to optimize the performance of the implemented TMD in the nacelle to lessen the vibrations of the offshore wind turbine tower, Ghassempour et al. [22] concluded that the ideal TMD tuning frequencies fluctuated with wind speed when the turbine was operating, but when it was parked, they matched the support structure's natural frequency. The technological and operational developments in offshore wind energy were highlighted in [23, 24], which also addressed issues such as cost, environmental impact, grid integration, and smart control strategies to enhance efficiency, collectively underscoring the global drive for optimizing offshore wind systems through technology and collaboration.

Alsaadi and Hamed [25], applied a PPF controller at resonance to curb tower vibrations, managed energy flow, and stabilized offshore wind turbines facing combined external forces. The researchers combined analytical, MSA, and numerical (Poincaré map) approaches, providing clear recommendations for stronger, more stable turbines in challenging ocean conditions. Elias and Beer [26] examined whether tuned mass damper-inerter systems fitted with electromagnetic generators can perform two functions simultaneously on offshore wind turbines: curb tower sway due to wind and waves and harvest extra energy. The results indicate that these devices could keep turbines steadier and boost their efficiency, even in harsh ocean conditions [27]. The authors presented a delayed-feedback control system that reduces the sway caused by wind and waves on floating offshore wind turbines, thereby lowering their energy costs. Simulations showed that the method could make the turbines steadier and more durable in rough sea conditions. According to Yang et al. [28], the latest techniques for monitoring and spotting problems in offshore turbine structures, both the towers and their foundations were reviewed. The authors demonstrated that these tools could make turbines safer, reduce maintenance costs, and extend their operational lifespan. Meanwhile, a new vibration-control scheme for turbine towers that blends two approaches: one based on "cubic negative velocity" and the other on "linear negative acceleration" was introduced by Amer et al. [29]. Eventually, Afridi et al. [30] delved into onshore, offshore, and floating wind turbines, inspecting their benefits, challenges, and environmental consequences. It explored how each type can contribute to clean energy while addressing issues like installation costs and ecological impacts. The research highlights the need for improved policies and technological innovations to enhance the efficiency and sustainability of wind energy. Ultimately, it offers insights to help shape a cleaner energy future. Both simulations and analytical models validated that this method not only boosted structural stability but also provided a feasible and affordable way to preserve wind turbine performance and safety.

It is essential for the forces applied through building nonlinear structures to be more realistic and appropriate for all worst climate circumstances. Therefore, Amer et al. [31] proposed a technique for accurately identifying the points of collapse for vibratory systems, enabling engineers to design enhanced stabilizers and dampers that suppress all unwanted oscillations. In addition, a special double pendulum, tracing a Lissajous curve, was analyzed to anticipate its stability and fluctuations through applying MSA [32]. Moreover, El-Sabaa et al. [33] handled the motion of a previous model attached to a rigid structure by adopting rigorous mathematical approaches to forecast its behavior in proximity to resonance, revealing outstanding agreement by comparing their theoretical predictions with computerized data. The interaction between the cart and pendulum was examined by Amer et al. [34] to predict the behavior closest to resonance using MSA, demonstrating that this interaction is efficiently controllable for preventing undesired disturbances. Elneklawy et al. [35] applied the parameterized feedback control torques to the satellite to achieve rapid stabilization. The behavior of a combined pendulum-oscillator mechanism connected to a piezoelectric transducer is investigated to supply perspectives for feasible energy harvesting sources [36, 37]. When adopting control units, such as negative derivative feedback (NDF) on a cart-pendulum [38], the researchers succeeded in settling down and retaining predictable behavior. A spherical pendulum and Duffing oscillator combined with a harvesting energy unit were analyzed by Abohamer et al. [39] to boost the excitation frequency and damping, which can significantly improve the performance of energy harvesting. The NIPPF controller is utilized in [40, 41] to lessen the harmful oscillations, enhancing the models' stability and performance.

In this work, a novel control strategy is proposed to manage energy flow and undesired vibrations of a single DOF in offshore wind turbine towers of the fundamental lateral bending mode under a wide range of simultaneous external excitations. We implemented a TD-NIPPF controller to mitigate harmful tower oscillations and enhance the model's overall performance while preserving stability. Among all perturbation strategies, we have applied the MSA to obtain second-order approximate solutions. Through a variety of classified resonance states, the examination of external and internal resonances is investigated. To evaluate the precision of the perturbation approach, numerical solutions are calculated, visually represented, and then compared with approximate solutions obtained employing the RK-4 method. The solvability conditions are established once the secular terms are eliminated, and all resonance cases are deduced. To explore steady-state behavior and check the stability of each fixed point, modulation equations are derived. Moreover, the force response and frequency response curves are visualized both before and after integrating the control device into the wind turbine system. Furthermore, we used the Routh-Hurwitz method, a precise technique for assessing system stability, to do a comprehensive stability analysis. In addition, we have identified a possible bifurcation diagram and LLE in critical resonance scenarios using methods such as the phase portrait approach and Poincaré maps to numerically estimate the impact of the most significant factors on the vibration behavior of the considered model. One method to reduce loading is to utilize structural control systems, which have been successfully applied in civil structures to improve structural response. For civil structures, the primary purpose of structural control systems is to increase inhabitant comfort by mitigating building accelerations. The proposed TD-NIPPF device not only reduced acceleration but also led to lessened fatigue loading. In wind turbine applications, fatigue is a design 1-driver, while fixed-bottom offshore platforms can benefit from structural control to reduce fatigue damage.

2. The Mathematical Simulation of the Offshore Wind Turbine

In this section, we simulated the mathematical modeling of the studied system, with the operational and structural components of the fundamental lateral bending mode of offshore wind turbines with fixed foundation settled in the seabed, shown in Fig. 1(a). At the same time, Figure 1(b) displays a schematic diagram of the impact of simultaneous multiple environmental forces on the structure. This assumption is commonly adopted due to the fact that the fundamental mode comprises most of the total structural response, especially in slender structures, including wind turbine towers. Further, the current study avoided higher-order oscillation modes (second and third bending), which correspond to conformation structures with additional nodes. Although these modes may participate in localized dynamical behavior, their effect on the overall response of slender offshore wind turbine towers is typically confined due to their higher natural frequencies and relatively low modal contribution factors, which enhance the dominance of the fundamental mode over higher ones, justifying the simplification of our model to be a single DOF approximation. In addition, we simplified the rotor-nacelle assembly to a concentrated mass at the top of the tower, and the associated blade-tower coupling interactions are not explicitly addressed, which is a standard and reasonable idealization for worldwide dynamical modeling where structural response is mainly governed by tower stiffness. Similarly, based on the assumption that the structure response is dominated by the fundamental mode, and the foundation stiffness is sufficiently substantial relative to the tower, the soil–structure interaction has been disregarded in the current analysis, which strongly confirms the significance of the fixed foundation in the model. Now, we can categorize the external forces into four groups: the wind forces (F_{aero} and F_W) affecting the major elements of the wind tower, which rely upon wind velocity, the wave force F_H affecting the bottom side of the wind tower, including the fixed-bottom offshore platform, to precisely determine the hydrodynamic wave force, where H stands for wave height. Eventually, the earthquake force F_{eqk}, which is one of the most powerful forces operating on the wind tower, is referred to as seismic excitation.

The GE that characterizes the structure under consideration, which is a single degree of freedom, was derived through [4]:

$$m\ddot{z}(t) + \varepsilon c\dot{z}(t) + kz(t) + \varepsilon F(t) = \varepsilon G(t), \tag{1}$$

where $z(t)$ refers to the structure's lateral displacement, the dot notation refers to the derivative with regard to time t, ε is a small parameter provided that $0 < \varepsilon << 1$, m is the mass of the structure, $F(t)$ refers to the total force acting on the tower, $G(t)$ refers to the proposed controller, c refers to the damping factor, and k refers to the stiffness parameter. Moreover, the total environmental forces can be modeled as $F(t) = F_{eqk} + F_{aero}\sin(\Omega_1 t) + F_H\cos(\Omega_2 t)\left|\cos(\Omega_2 t)\right|$ such that Ω_1, Ω_2 are the dominant excitation frequencies of the wind and wave forces, and the gain signal will be addressed by the TD-NIPPF controller. Now, we are going to describe the upcoming parameters in the dimensionless form:

$$\mu_1 = \frac{c}{m},\ \omega_1^2 = \frac{k}{m},\ f_{eqk} = \frac{F_{eqk}}{m},\ f_a = \frac{F_{aero}}{m},\ f_h = \frac{F_H}{m}. \tag{2}$$

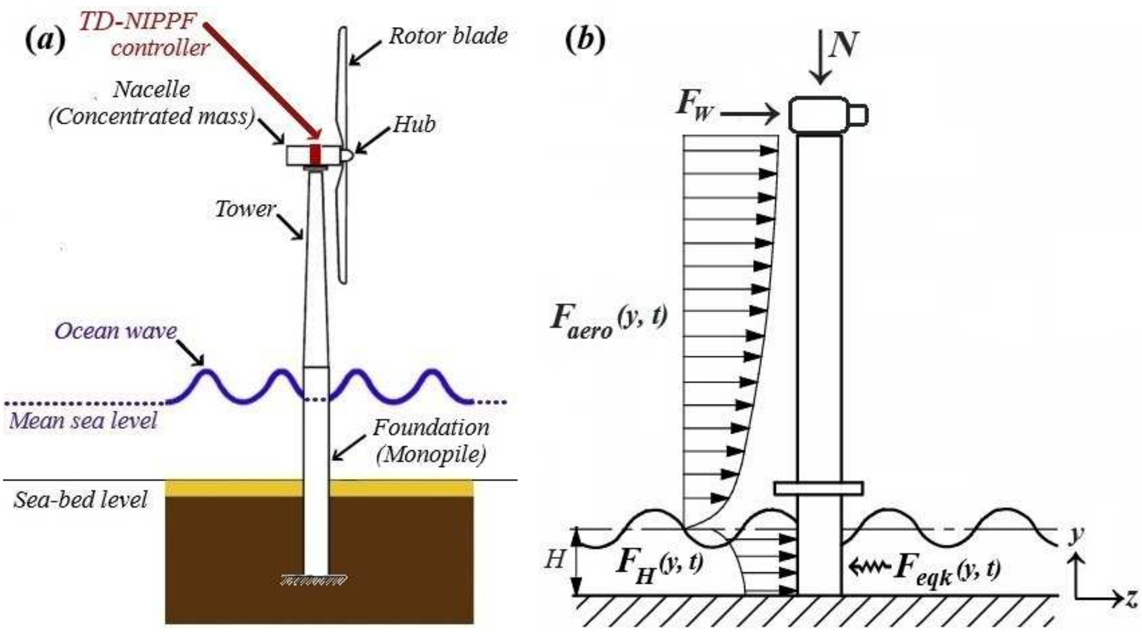

Fig. 1. (a) Schematic diagram of the offshore wind turbine tower with TD-NIPPF controller, (b) Distribution of loads affecting the investigated model.

Here, μ_1 is the damping factor of the original system associated with the first mode, ω_1 is the natural frequency of the tower system, f_a and f_h are the amplitudes of wind and wave forces, and $f_{eqk} = \alpha \cos(\pi t)$ is the amplitude of the idealized harmonic seismic wave. In addition, the mathematical formulation of the proposed loading excitation is developed for reduced-order parametric evaluation of the structural response and is not designed to reproduce the entire stochastic spectral characteristics of wind and wave loading or the fluctuating broadband nature of actual earthquake ground motions. Consequently, this reduction is appropriate for a detailed assessment of resonance impacts and coupled vibration features within the adopted single DOF structure, and examining the sensitivity of the model to the associated excitation frequency.

Then, substituting from Eq. (2) into Eq. (1), the GE of the system in the dimensionless format will be:

$$\ddot{z} + \varepsilon\,\mu_1\,\dot{z} + \omega_1^2\,z + \varepsilon f_{eqk} + \varepsilon f_a \sin(\Omega_1 t) = \varepsilon\, f_h \cos(\Omega_2 t)\left|\cos(\Omega_2 t)\right|. \tag{3}$$

To regulate unwanted tower oscillations, we implemented a TD-NIPPF control device in the system under investigation, as addressed by Eqs. (5) and (6). Besides, the tower structure supplies the TD-NIPPF device with the feedback signal through the signal diagram displayed in Fig. 2, and the GE in Eq. (3) will be formulated regarding the TD-NIPPF device as:

$$\ddot{z} + \varepsilon\,\mu_1\,\dot{z} + \omega_1^2\,z + \varepsilon\,\alpha\cos(\pi t) + \varepsilon f_a \sin(\Omega_1 t) = \varepsilon\, f_h \cos(\Omega_2 t)\left|\cos(\Omega_2 t)\right| + \varepsilon\,\beta_1\, y(t-\tau) + \varepsilon\,\beta_2\,\varphi(t), \tag{4}$$

$$\ddot{y} + \varepsilon\,\mu_2\,\dot{y} + \omega_2^2\,y = \varepsilon\,\beta_3\, z(t-\tau), \tag{5}$$

$$\dot{\varphi} + \mu_3\,\varphi = \beta_4\, z(t). \tag{6}$$

Here μ_2, μ_3 are the damping factors of the NIPPF controller, $\beta_1, \beta_2, \beta_3$, and β_4 are the controller parameters, τ is the time delay and ω_2 is the natural frequency of the control unit.

3. Perturbation Methodology

In this section, we will use the MSA to solve Eqs. (4) to (6) and obtain the approximate solutions we're looking for. This approach splits the model's timeline into different time-scales, making it a strong tool for analyzing nonlinear differential equations (DEs). It's a powerful way to better understand complex systems, leading to more precise and methodical approximations. To ensure these solutions are valid and consistent, we need to eliminate any terms that grow indefinitely over time, known as 'secular terms'. To do this, we'll express the functions z, y, and f in a power series that depends on a small parameter ε that's been used successfully before [31, 32]:

$$\begin{aligned} z(t,\varepsilon) &= z_0(T_0,T_1) + \varepsilon\, z_1(T_0,T_1) + O(\varepsilon^2), \\ y(t,\varepsilon) &= y_0(T_0,T_1) + \varepsilon\, y_1(T_0,T_1) + O(\varepsilon^2), \\ \varphi\ (t,\varepsilon) &= \varphi_0(T_0,T_1) + \varepsilon\,\varphi_1(T_0,T_1) + O(\varepsilon^2), \end{aligned} \tag{7}$$

where $T_n = \varepsilon^n t\ (n = 0,1)$ assign proposed time scales in which T_0 represents the fast scale and T_1 simulates the slower one. Thus, the derivatives involved in Eqs. (4), (5), and (6) should be transformed into new ones in terms of T_n according to the following operators, after omitting the terms of $O(\varepsilon^2)$ and higher orders:

$$\begin{aligned} \frac{d}{dt} &= D_0 + \varepsilon\, D_1, \\ \frac{d^2}{dt^2} &= D_0^2 + 2\,\varepsilon D_0\, D_1 + O(\varepsilon^2). \end{aligned} \tag{8}$$

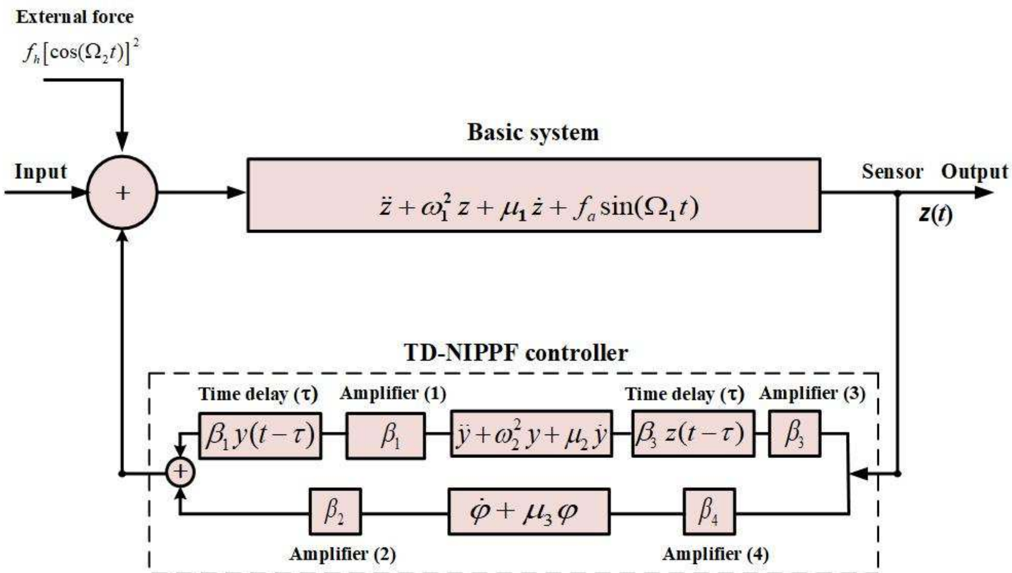

Fig. 2. Block diagram for the TD-NIPPF controller of the dynamical model.

Here, $D_n = \partial / \partial T_n$, $n = 0, 1$ are the derivatives related to the newly mentioned scales. Moreover, it is essential to define the variables associated with the time delay $z(t-\tau)$, $y(t-\tau)$ due to the following form:

$$\begin{aligned} z(t-\tau) &= z_0(t-\tau) + \varepsilon\, z_1(t-\tau) + O(\varepsilon^2) \;, \quad & y(t-\tau) &= z_0(t-\tau) + \varepsilon\, z_1(t-\tau) + O(\varepsilon^2) \\ &= z_{0\tau} + \varepsilon\, z_{1\tau} + O(\varepsilon^2) & &= y_{0\tau} + \varepsilon\, y_{1\tau} + O(\varepsilon^2). \end{aligned} \tag{9}$$

Utilizing the above-mentioned variables in Eq. (7) and (9), and derivatives in Eq. (8) into the GEs of Eqs. (4), (5), and (6), then equating the coefficients of similar powers of the general, yields six partial DEs as:

(i) Order of ε^0:

$$(D_0^2 + \omega_1^2)\; z_0 = 0, \tag{10}$$

$$(D_0^2 + \omega_2^2)\; y_0 = 0, \tag{11}$$

$$(D_0 + \mu_3)\,\varphi_0 = \beta_4\, z_0. \tag{12}$$

(ii) Order of ε^1:

$$(D_0^2 + \omega_1^2)\; z_1 = -\,2\, D_0 D_1\, z_0 - \mu_1\, D_0\, z_0 - \frac{f_a}{2\,i}\,(e^{i\,\Omega_1 T_0} - e^{-i\,\Omega_1 T_0}) - \frac{\alpha}{2}(e^{i\,\pi\,T_0} + e^{-i\,\pi\,T_0}) + \frac{f_h}{4}\,(e^{2\,i\,\Omega_2\,T_0} + e^{-2\,i\,\Omega_2\,T_0} + 2) + \beta_1\, y_{0\tau} + \beta_2\,\varphi_0\,, \tag{13}$$

$$(D_0^2 + \omega_2^2)\; y_1 = -2D_0\, D_1\, y_0 - \mu_2\, D_0\, y_0 + \beta_3\, z_{0\tau}\,, \tag{14}$$

$$(D_0 + \mu_3)\,\varphi_1 = -D_1\,\varphi_0 + \beta_4\, z_1. \tag{15}$$

It is noticeable that Eqs. (10) and (11) are homogeneous, while Eq. (12) is nonhomogeneous; therefore, the general solutions of each can be obtained, respectively, as:

$$z_0 = A(T_1)\, e^{i\omega_1 T_0} + \bar{A}(T_1)\, e^{-\,i\omega_1 T_0}, \tag{16}$$

$$y_0 = B(T_1)\, e^{i\omega_2 T_0} + \bar{B}(T_1)\, e^{-\,i\omega_2 T_0}, \tag{17}$$

$$\varphi_0 = \frac{\beta_4\, A(T_1)}{\mu_3 + i\omega_1}\, e^{i\omega_1 T_0} + \frac{\beta_4\, \bar{A}(T_1)}{\mu_3 - i\omega_1}\, e^{-\,i\omega_1 T_0}. \tag{18}$$

Here, A and B indicate to anonymous complex functions that can be fully determined later through the outcome of secular terms, while $\bar{A}$ and $\bar{B}$ display their complex conjugate.

Depending on the previous solutions of the initial (zero) approximations, it is necessary to express the variables related to the time delay, such as:

$$\begin{aligned} z_{0\tau} &= z_0(t-\tau) = A_\tau(\varepsilon(t-\tau))\;\; e^{i\omega_1 (T_0-\tau)} + \bar{A}_\tau(\varepsilon(t-\tau))\;\; e^{-\,i\omega_1 (T_0-\tau)}, \\ y_{0\tau} &= y_0(t-\tau) = B_\tau(\varepsilon(t-\tau))\;\; e^{i\omega_2 (T_0-\tau)} + \bar{B}_\tau(\varepsilon(t-\tau))\;\; e^{-\,i\omega_2 (T_0-\tau)}. \end{aligned} \tag{19}$$

where $A_\tau(\varepsilon\,(t-\tau)) = A_\tau(\varepsilon t - \tau) = A_\tau(T_1 - \varepsilon\,\tau)$, $B_\tau(\varepsilon(t-\tau)) = B_\tau(\varepsilon t - \tau) = B_\tau(T_1 - \varepsilon\,\tau)$. Employing the Taylor series to enlarge $A_\tau(T_1 - \varepsilon\,\tau)$ and $B_\tau(T_1 - \varepsilon\,\tau)$, keeping the first term in both for simplicity, to get:

$$\begin{aligned} z_0(t-\tau) &= A_\tau(T_1)\;\; e^{i\omega_1 (T_0-\tau)} + \bar{A}_\tau(T_1)\;\; e^{-\,i\omega_1 (T_0-\tau)}, \\ y_0(t-\tau) &= B_\tau(T_1)\;\; e^{i\omega_2 (T_0-\tau)} + \bar{B}_\tau(T_1)\;\; e^{-\,i\omega_2 (T_0-\tau)}. \end{aligned} \tag{20}$$

Here, A_τ, B_τ and their conjugates point out unknown complex functions. Besides, these functions will be approached to A, B when applying the expansion of the Taylor series. Eventually, dropping the secular terms in Eqs. (13) to (15) and plugging Eqs. (16) to (20) in that equation, the first-order approximations z_1, y_1 and f_1 will be reformed as:

$$\begin{aligned} z_1 = {} & C(T_1)\, e^{i\omega_1 T_0} + \bar{C}(T_1)\, e^{-\,i\omega_1 T_0} + \frac{i f_a}{2(\omega_1^2 - \Omega_1^2)}\,(e^{i\,\Omega_1\,T_0} - e^{-i\,\Omega_1\,T_0}) + \frac{f_h}{2\,\omega_1^2} + \frac{f_h}{4(\omega_1^2 - 4\,\Omega_2^2)}\,(e^{2\,i\,\Omega_2\,T_0} + e^{-2\,i\,\Omega_2\,T_0}) \\ & + \frac{\beta_1}{\omega_1^2 - \omega_2^2}\,(B\, e^{i\omega_2 (T_0-\tau)} + \bar{B}\, e^{-\,i\omega_2 (T_0-\tau)}) - \frac{\alpha}{2(\omega_1^2 - \pi^2)}(e^{i\,\pi\,T_0} + e^{-i\,\pi\,T_0}), \end{aligned} \tag{21}$$

$$y_1 = D(T_1)\, e^{i\omega_2 T_0} + \bar{D}(T_1)\, e^{-\,i\omega_2 T_0} + \frac{\beta_3}{\omega_2^2 - \omega_1^2}\,(A\, e^{i\omega_1 (T_0-\tau)} + \bar{A}\, e^{-\,i\omega_1 (T_0-\tau)}), \tag{22}$$

$$\begin{aligned} \varphi_1 = {} & \frac{\beta_4}{\mu_3 + i\omega_1}\,(C - \frac{D_1 A}{\mu_3 + i\omega_1})\, e^{i\omega_1 T_0} + \frac{\beta_4}{\mu_3 - i\omega_1}\,(\bar{C} - \frac{D_1 \bar{A}}{\mu_3 - i\omega_1})\, e^{-\,i\omega_1 T_0} + \frac{i f_a\, \beta_4}{2\left(\omega_1^2 - \Omega_1^2\right)}\,(\frac{e^{i\,\Omega_1\,T_0}}{\mu_3 + i\,\Omega_1} - \frac{e^{-i\,\Omega_1\,T_0}}{\mu_3 - i\,\Omega_1}) + \frac{f_h\,\beta_4}{2\mu_3\,\omega_1^2} \\ & + \frac{f_h\,\beta_4}{4\left(\omega_1^2 - 4\,\Omega_2^2\right)}\,(\frac{e^{2\,i\,\Omega_2\,T_0}}{\mu_3 + 2\,i\,\Omega_2} + \frac{e^{-2\,i\,\Omega_2\,T_0}}{\mu_3 - 2\,i\,\Omega_2}) + \frac{\beta_1\,\beta_4}{\omega_1^2 - \omega_2^2}\,(\frac{B\, e^{i\omega_2 (T_0-\tau)}}{\mu_3 + i\omega_2} + \frac{\bar{B}\, e^{-\,i\omega_2 (T_0+\tau)}}{\mu_3 - i\omega_2}). \end{aligned} \tag{23}$$

Here C and D represent anonymous complex functions, while $\bar{C}$ and $\bar{D}$ denote the corresponding complex conjugate included in Eqs. (21) to (23). The previous approximate solutions, which were computationally determined, enabled us to obtain precise predictions of frequency ranges, device designs, and load levels, thereby avoiding devastating breakdowns such as the worst resonance states and guiding us in making the model structure more reliable and realistic.

4. Resonance States Investigation

The current division confines the possible resonance states at which the validation of accomplished asymptotic solutions (21) to (23) will be verified when their denominators diverge from zero [33]. These states fall into three types:

- Primary external resonance state at $\Omega_1 \approx \pm\, \omega_1$,
- Super-harmonic resonance state at $\Omega_2 \approx \pm\, 0.5\, \omega_2$,
- Internal resonance state at $\omega_2 \approx \pm \omega_1$.

It is strictly apparent that the closeness of oscillation of the system under consideration to any previous resonance state might harm the conductance and cause it to depart from the stability zone. For that reason, we extremely prioritize the worst state, which involves a blend of the primary external state $\Omega_1 \approx \omega_1$ and internal one $\omega_2 \approx \omega_1$. Additionally, synchronization between these two resonances should be considered to maximize our goal. Next, it is required to characterize how close both resonances Ω_1 and ω_2 to ω_1 through the insertion of the detuning parameters σ_r $(r = 1,2)$ that measures the deviation between successive vibrations and the strict resonance as [34]:

$$\Omega_1 = \omega_1 + \varepsilon\, \sigma_1 \quad , \quad \omega_2 = \omega_1 + \varepsilon\, \sigma_2 . \tag{24}$$

Thus, plugging Eqs. (16) to (20) and (24) into first-order approximations (13) to (15), the solvability limitations will be recognized as a result of omitting the output secular terms:

$$\frac{i f_a}{2} e^{i \sigma_1 T_1} + \beta_1 B\, e^{i(\sigma_2 T_1 - \omega_2 \tau)} - i\,\omega_1 \Big(2\frac{\partial A}{\partial T_1} + \mu_1 A\Big) = 0, \tag{25}$$

$$\beta_3 A\, e^{-i(\sigma_2 T_1 + \omega_1 \tau)} - i\,\omega_2 \Big(2\frac{\partial B}{\partial T_1} + \mu_2 B\Big) = 0. \tag{26}$$

Switching the latest generated conditions into polar format yields four nonlinear partial DEs regarding the anonymous functions A and B through the rule according to [43]:

$$A(T_1) = \frac{a(T_1)}{2}\, e^{i\,\psi_1(T_1)} \;;\quad B(T_1) = \frac{b(T_1)}{2}\, e^{i\,\psi_2(T_1)}. \tag{27}$$

Here, a, b describe the amplitudes of the investigated model and ψ_1, ψ_2 represent the corresponding phases. Conditions (25) and (26) should be turned into ordinary DEs through the introduction of updated phases θ_1, θ_2 that are defined as:

$$\theta_1(T_1) = T_1 \sigma_1 - \psi_1(T_1)\,, \qquad \theta_2(T_1) = T_1 \sigma_2 - \psi_1(T_1) + \psi_2(T_1). \tag{28}$$

Then, plugging Eqs. (27) and (28) into Eqs. (25) and (26) and isolating the real and imaginary parts leads us to a set of four first-order ODEs concerning the amplitudes a, b and updated phases θ_1, θ_2 which is identified as modulation equations in the form:

$$\begin{aligned}
\dot{a} &= -\frac{\mu_1 a}{2} + \frac{\beta_1 b}{2\omega_1}\sin(\theta_2 - \omega_2 \tau) + \frac{f_a}{2\omega_1}\cos\,\theta_1\,,\\
a\,\dot{\theta}_1 &= a\,\sigma_1 + \frac{\beta_1 b}{2\omega_1}\cos(\theta_2 - \omega_2\tau) - \frac{f_a}{2\omega_1}\sin\,\theta_1\,,\\
\dot{b} &= -\frac{\mu_2 b}{2} - \frac{\beta_3 a}{2\omega_2}\sin(\theta_2 + \omega_1\tau)\,,\\
b\,\dot{\theta}_2 &= b\,\sigma_2 - \frac{\beta_3 a}{2\omega_2}\cos(\theta_2 + \omega_1\tau) + \frac{\beta_1 b^2}{2\omega_1 a}\cos(\theta_2 - \omega_2\tau) - \frac{f_a b}{2\omega_1 a}\sin\,\theta_1 .
\end{aligned} \tag{29}$$

The numerical solution of the preceding modular system can be extracted via the RK-4 methodology to illustrate graphically the time variation for the amplitudes a, b at resonance in case of the absence and presence of the controller, regarding data and initial conditions listed below:

$$\begin{aligned}
&\mu_1 = 0.04, \mu_2 = 0.02, \mu_3 = 0.02, \beta_1 = 3, \beta_2 = 0.1, \beta_3 = 0.5, \beta_4 = 0.015, \omega_1 = 1.26, \omega_2 = 1.26,\\
&\Omega_1 = 1.26, \Omega_2 = 0.4, f_a = 7, f_h = 5, a(0) = 0.03, b(0) = 0.05, \alpha = 8, \varepsilon = 1, \tau = 0.015.
\end{aligned}$$

According to the preceding parameters, Figs. (3) to (7) are plotted, such as Fig. (3), which demonstrates the structure's oscillation $z(t)$ behavior before and after applying the TD-NIPPF controller at resonant states. Further, the damping coefficient is taken to be small, consistent with weakly damped slender structures, while the excitation amplitudes are selected to reflect moderate environmental loading conditions. Initially, the response of the red curve exhibits a distinct divergence over time in the absence of the controller $(\beta_1 = 0, \beta_2 = 0, \beta_3 = 0, \beta_4 = 0)$, reflecting unstable and widening oscillations leads to entire harm to the wind structure. After introducing the TD-NIPPF controller $(\beta_1 = 3, \beta_2 = 0.5, \beta_3 = 0.5, \beta_4 = 0.015)$, the structure's response of the blue curve stabilizes considerably, maintaining tiny amplitude oscillations around zero. This demonstrates the controller's effectiveness in suppressing excessive oscillations and enhancing structural stability.

To explore how the time delay affects reducing harm oscillations, Fig. (4) introduces the time history of the solution at resonance states in the presence of the TD-NIPPF controller at different values of time delay. Basically, we deduced that the system's amplitude in the case of $\tau = 0$, which is diagrammed in purple, and is close in magnitude compared to $\tau = 0.004$ and $\tau = 0.015$, which are plotted in red and black, respectively.

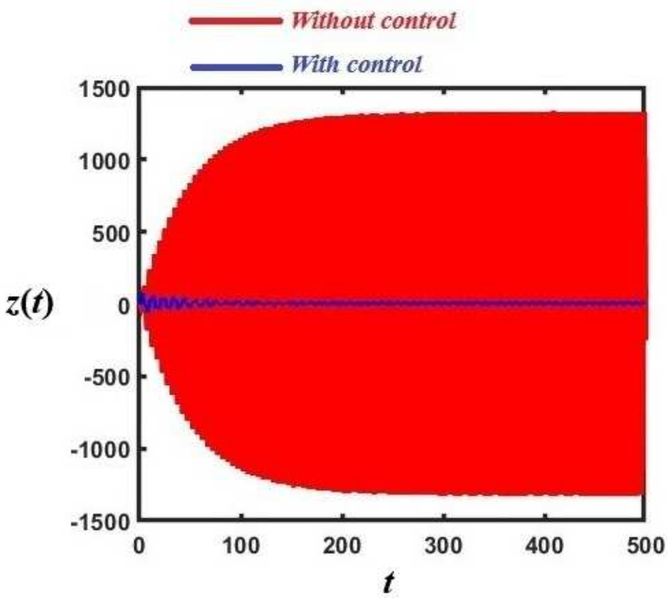

Fig. 3. Time-response solution z(t) at resonance states $\Omega_1 \approx \omega_1, \omega_2 \approx \omega_1$ with and without TD-NIPPF control.

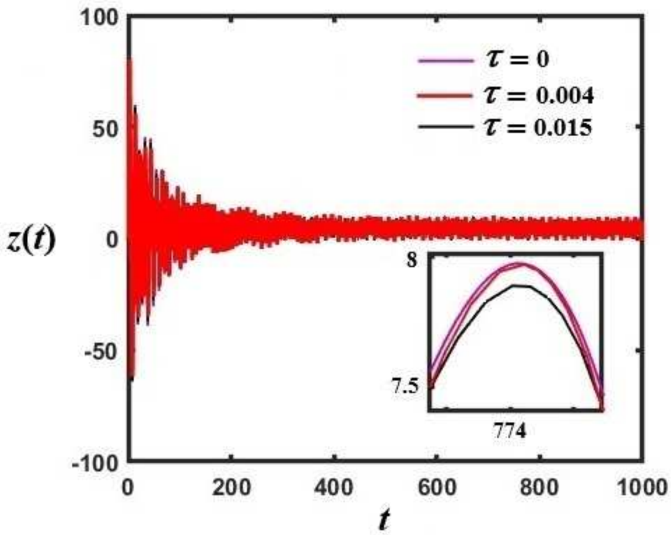

Fig. 4. Demonstrate the time-response solution z(t) at resonant states ($\Omega_1 \approx \omega_1, \omega_2 \approx \omega_1$) with control, indicating the influence of different time delay values.

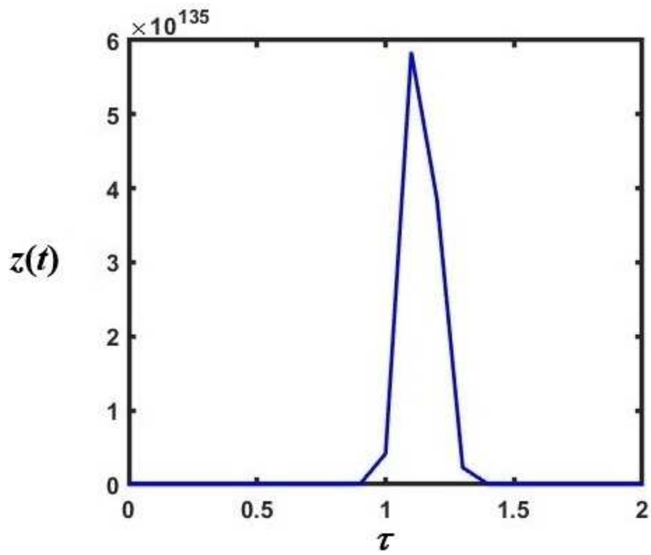

Fig. 5. Model amplitude z(t) versus time delay.

Table 1. Comparison of vibration attenuation and control effectiveness of the TD-NIPPF controller for different time delays.

Controller patterns	Amplitude without control	Amplitude with control	Controller effect = E (times)	Controller effectiveness (%)
TD-NIPPF with (τ = 0)	1326.65	9.56	138.77	99.2
TD-NIPPF with (τ = 0.004)	1326.65	8.6	154.26	99.3
TD-NIPPF with (τ = 0.015)	1326.65	6.756	196.36	99.5

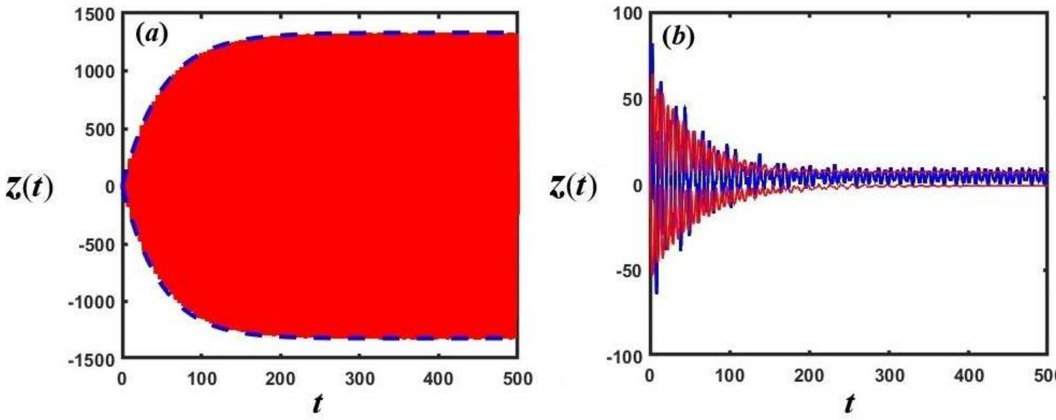

Fig. 6. Comparison between numerical solution, portrayed by blue curve, and approximate solution, portrayed by red curve, at resonant states ($\Omega_1 \approx \omega_1, \omega_2 \approx \omega_1$) in case of: (a) Without control ($\beta_1 = 0, \beta_2 = 0, \beta_3 = 0, \beta_4 = 0$), (b) With TD-NIPPF control ($\beta_1 = 3, \beta_2 = 0.5, \beta_3 = 0.5, \beta_4 = 0.015$).

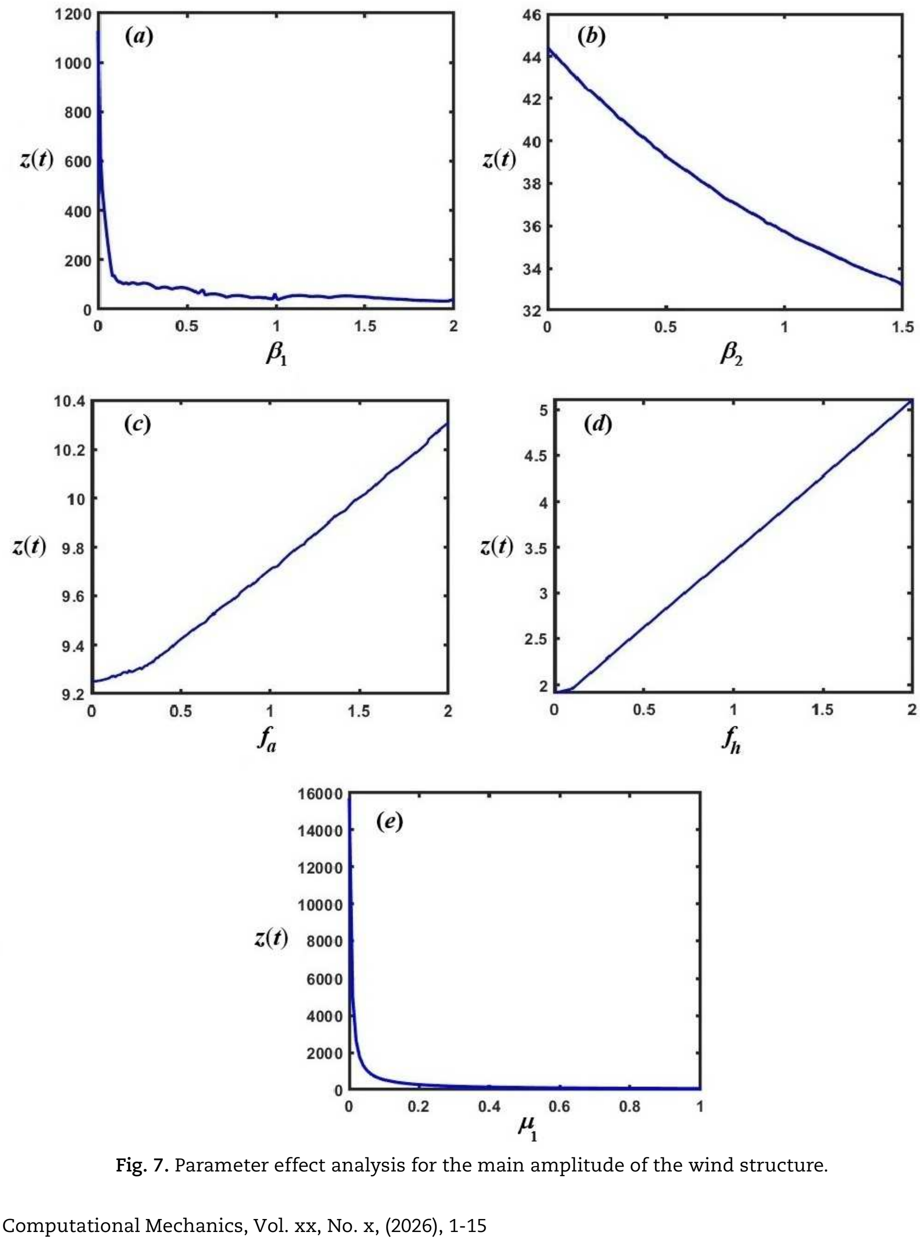

Fig. 7. Parameter effect analysis for the main amplitude of the wind structure.

Moreover, we utilized the time delay to enhance the reliability and practicality of our work, thereby facilitating the adequate performance of the TD-NIPPF controller. Furthermore, the effectiveness of the TD-NIPPF controller can be confined in Table 1.

Figure 5 characterizes the variation in amplitude over time delay scenarios that mitigate violent structural oscillations caused by wind turbines. It also defines the boundaries of the region where specific time delay values, ranging as $\tau \in$ [0, 0.9001] and [1.4001, 2], effectively decrease amplitude, boost the efficiency of the proposed controller, and avoid the zone (0.9001 , 1.4001) where time delay may lose its functionality and act as an external force. On the other hand, Fig. 6(a) portrays a comparison between the numerical solution based on the RK-4 method and the analytic solution generated via the MSA, at resonance states without control. In contrast, Fig. 6(b) portrays the same comparison with the control. Both reflect a significant level of consistency between the approximate and numerical solution and verify a remarkable precision of the MSA.

Now, let's look at how the wind structure parameters $\mu_1, \beta_1, \beta_2, f_h$, and f_a affect the amplitude fluctuations of $z(t)$. Interestingly, as μ_1, β_1, and β_2 increase, the magnitude of $z(t)$ decreases, this is clearly illustrated in Figs. 7(a), (b), and (e). On the other hand, as apparent in Figs. 7(c) and (d), the amplitude of $z(t)$ climbs as f_a and f_h goes up.

5. Steady-State Analysis

In this section, we will examine the output oscillations produced by the system under examination, focusing specifically on its steady-state solutions. As the system's damping reduces transient fluctuations, steady-state case becomes more noticeable and making this analysis a key to understanding the system's behavior. The main point here is to firstly extract a set of two nonlinear algebraic equations from the earlier set by eliminating the derivatives of the amplitudes and updated phases [36]. Then, system (29) will be transformed to:

$$\begin{aligned}
\frac{\mu_1 a}{2} &= \frac{\beta_1 b}{2\omega_1}\sin(\theta_2 - \omega_2\tau) + \frac{f_a}{2\omega_1}\cos\theta_1, \\
a\,\sigma_1 &= \frac{-\beta_1 b}{2\omega_1}\cos(\theta_2 - \omega_2\tau) + \frac{f_a}{2\omega_1}\sin\theta_1, \\
\frac{\mu_2 b}{2} &= \frac{-\beta_3 a}{2\omega_2}\sin(\theta_2 + \omega_1\tau), \\
b\,(\sigma_2 - \sigma_1) &= \frac{\beta_3 a}{2\omega_2}\cos(\theta_2 + \omega_1\tau).
\end{aligned} \tag{30}$$

Once the updated phases θ_1, θ_2 are gone, the frequency-response equations, which are made up of two algebraic equations regarding the detuning parameters σ_r, will eventually be generated as:

$$a^2 = \frac{\omega_2^2}{\beta_3^2}\,[\mu_2^2 + 4(\sigma_2 - \sigma_1)^2]\; b^2. \tag{31}$$

$$\beta_1^2 b^2 = \omega_1^2 a^2(\mu_1^2 + \sigma_1^2) - f_a^2 + 2 f_a\,\beta_1\, b\sin(\omega_1\tau). \tag{32}$$

Equations (32) have been obtained for small phases θ_1, θ_2. Secondly, to seek out the stability of the associated steady-state solutions near the fixed points, we propose that the amplitudes and phases tend to be:

$$\begin{aligned}
a &= a_{10} + a_{11}, \quad & b &= b_{10} + b_{11}, \\
\theta_1 &= \theta_{10} + \theta_{11}, \quad & \theta_2 &= \theta_{20} + \theta_{21},
\end{aligned} \tag{33}$$

where the steady-state solutions are symbolized by $a_{10}, b_{10}, \theta_{10}$, and θ_{20}, even as the slight perturbations relative to the previous solutions are indicated by $a_{11}, b_{11}, \theta_{11}$, and θ_{21}. The subsequent ODE system can be extracted after linearization by substituting Eq. (33) into Eq. (29) to get the next form:

$$\begin{pmatrix} \dot a_{11} \\ \dot\theta_{11} \\ \dot b_{11} \\ \dot\theta_{21} \end{pmatrix} = J \begin{pmatrix} a_{11} \\ \theta_{11} \\ b_{11} \\ \theta_{21} \end{pmatrix} = \begin{pmatrix} \gamma_{11} & \gamma_{12} & \gamma_{13} & \gamma_{14} \\ \gamma_{21} & \gamma_{22} & \gamma_{23} & \gamma_{24} \\ \gamma_{31} & \gamma_{32} & \gamma_{33} & \gamma_{34} \\ \gamma_{41} & \gamma_{42} & \gamma_{43} & \gamma_{44} \end{pmatrix} \begin{pmatrix} a_{11} \\ \theta_{11} \\ b_{11} \\ \theta_{21} \end{pmatrix}. \tag{34}$$

Such that J is referred to as the Jacobian matrix, and its components are overviewed in the Appendix. The associated eigenvalues of the earlier matrix J will be calculated through finding the roots of the following fourth-order characteristic equation:

$$\lambda^4 + \Gamma_1\lambda^3 + \Gamma_2\lambda^2 + \Gamma_3\lambda + \Gamma_4 = 0, \tag{35}$$

where the coefficients Γ_r $(r = 1, 2, 3, 4)$ are functions of $a_{10}, b_{10}, \theta_{10}, \theta_{20}, \beta_1, \beta_3, \omega_1, \omega_2, \mu_1, \mu_2, f_a$ and τ (see the Appendix). In most cases, the sign of the real parts of the roots of the previous characteristic equation, which Routh-Hurwitz develops, determines how stable the fixed solutions that are generated will be. According to the Routh-Hurwitz technique, a positive sign indicates that the fixed solutions will be unstable. Otherwise, the fixed solutions will be stable, verifying the following conditions [37]:

$$\begin{aligned}
&\Gamma_1 > 0, \qquad & &\Gamma_3(\Gamma_1\Gamma_2 - \Gamma_3) - \Gamma_4\Gamma_1^{\,2} > 0, \\
&\Gamma_1\Gamma_2 - \Gamma_3 > 0, \qquad & &\Gamma_4 > 0.
\end{aligned} \tag{36}$$

By analyzing the resonant response curves in Figs. (8) to (10), which are calculated from Eqs. (31) and (32), we can pinpoint where the system stays stable (solid lines) or veers into instability (dashed lines). Stable zones mean steady, predictable responses under forcing, while unstable ones risk chaotic or runaway reactions due to nonlinear effects.

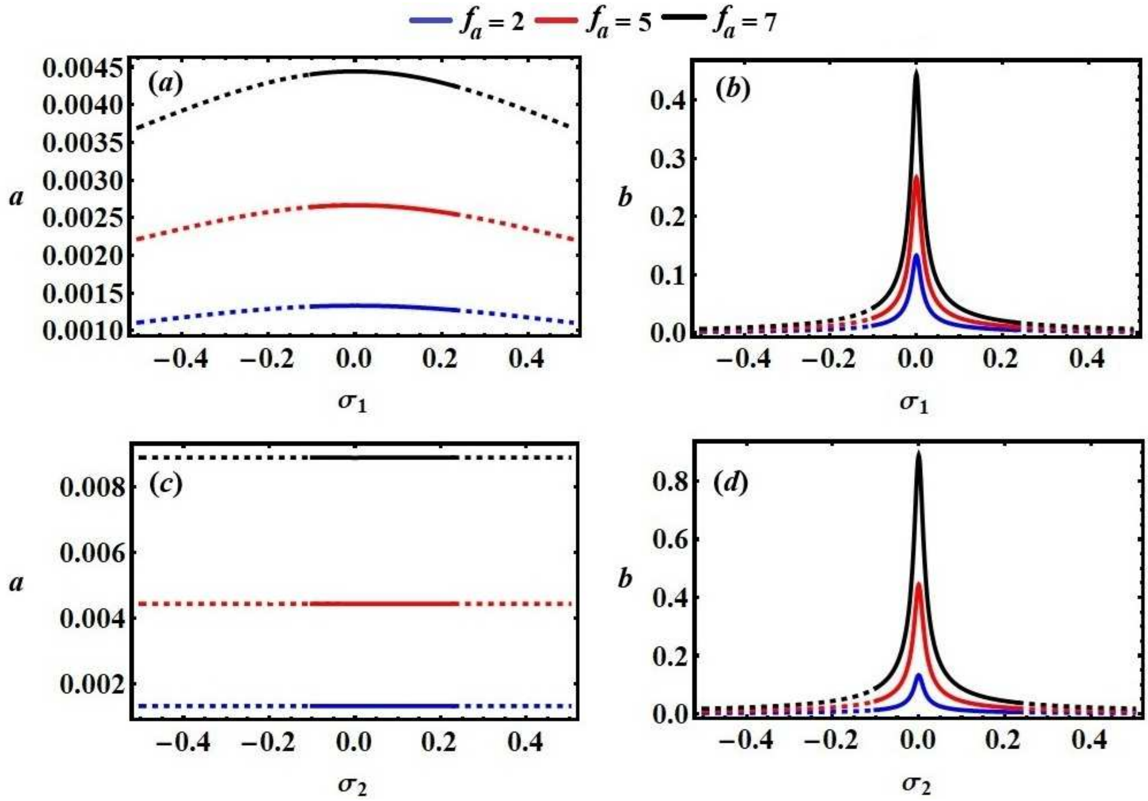

Fig. 8. Resonance curves for the amplitudes a, b versus σ_1, σ_2 in case of specific values of f_a at ($\beta_1 = 3, \beta_2 = 0.1, \beta_3 = 0.5, \beta_4 = 0.015$).

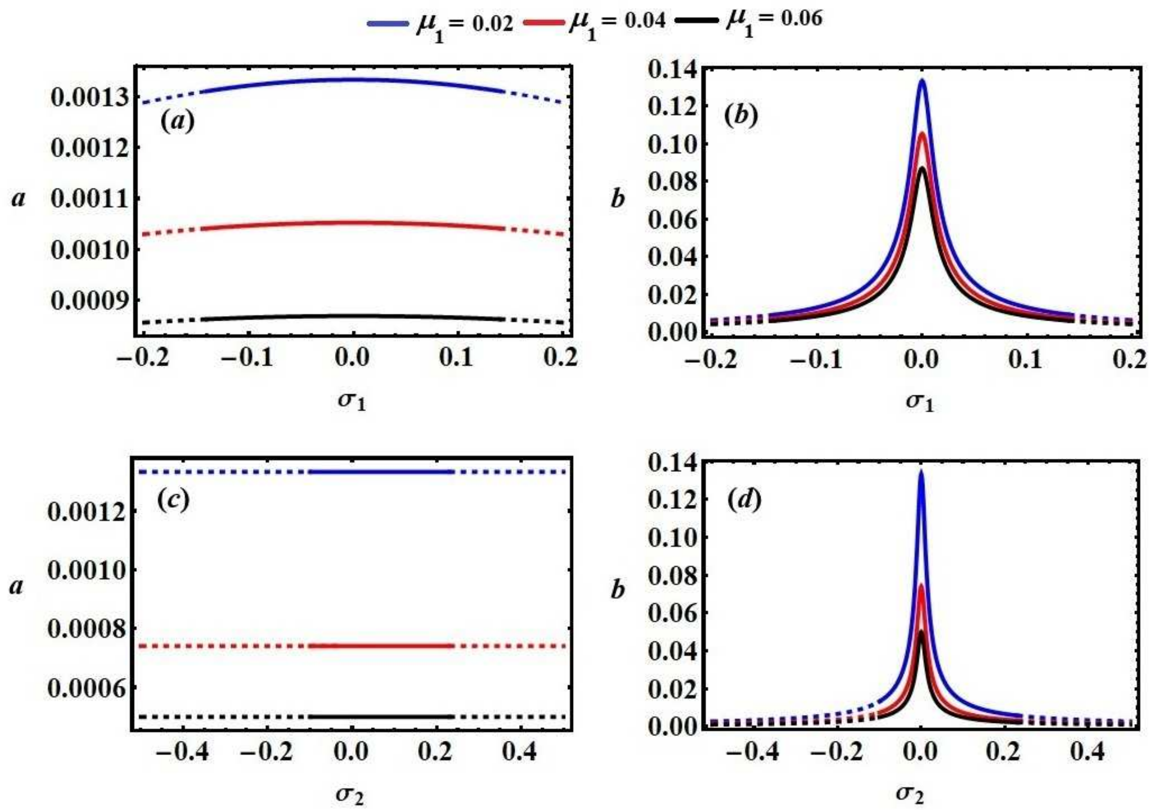

Fig. 9. Resonance curves for the amplitudes a, b versus σ_1, σ_2 in case of specific values of μ_1 at ($\beta_1 = 3, \beta_2 = 0.1, \beta_3 = 0.5, \beta_4 = 0.015$).

We found that key stability factors, like the forcing coefficient f_a, damping coefficient μ_1, and controller gain β_1 which really make a difference in whether the system stays stable. The resonance curves portrayed in Fig. 8 demonstrate that as we increase the forcing coefficient $f_a = (2,5,7)$, the system's oscillations grow larger in amplitude. With low forcing $f_a = 2$, the response remains stable, while higher forcing $f_a = 7$ creates significant peaks and possible instability near resonance. When the lines switch from solid to dashed, that's your red flag, it means that the forces are getting too strong for the damp to handle, and the system could fail. Therefore, for optimal performance, it is best to steer clear of the unstable dashed zones.

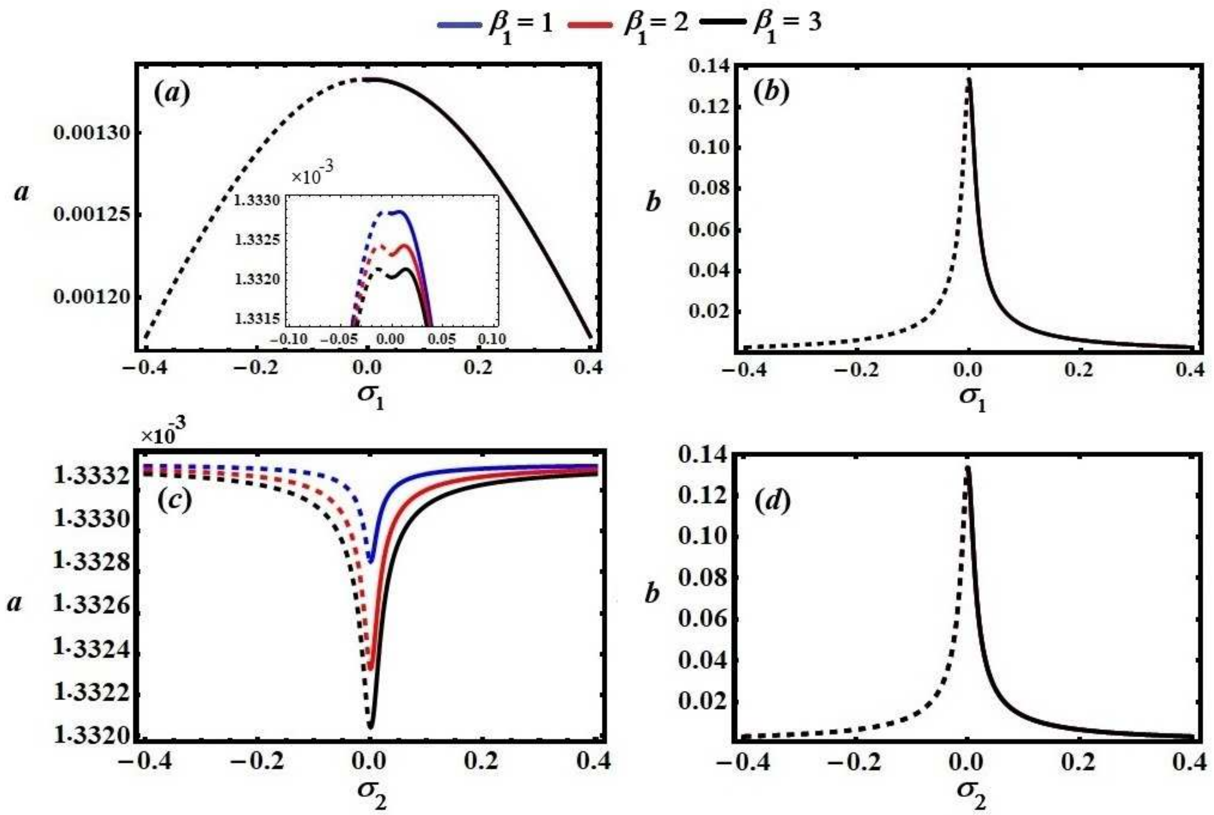

Fig. 10. Resonance curves for the amplitudes a, b versus σ_1, σ_2 in case of specific values of β_1 at ($\beta_2 = 0.1$, $\beta_3 = 0.5$, $\beta_4 = 0.015$).

In contrast, the resonance curves, plotted in Fig. 9 show that as the damping coefficient μ_1 grows from 0.02 to 0.06, the peak amplitude of resonance mitigates, indicating energy dissipation. The curves also broaden, demonstrating a wider frequency range over which significant vibration occurs. Higher damping $\mu_1 = 0.06$ results in a more flattened and stabilizing response, while lower damping $\mu_1 = 0.02$ produces sharper, more pronounced peaks. Besides, Fig. 10 confirms that the controller parameter β_1 effectively suppresses resonant amplitudes and disperses energy over a broader frequency band to avoid destructive resonance as a varies with σ_1, with no effect in the case of b.

The resonance curves introduced a direct physical characterization of the model behavior adjacent to the stability boundaries. Also, it is noted that the amplitudes a and b remain bounded away from resonance, whereas considerable amplification occurs in the vicinity of $\sigma_1 = 0$, $\sigma_2 = 0$, which corresponds to the primary resonance condition. Among the two response components, b exhibits the strongest sensitivity, with noticeable peaks that signify a significant vulnerability to dynamic amplification and potential loss of stability. Further, these observations are consistent with the analytical stability conditions. Specifically, the regions of high-amplitude response in the resonance curves correspond to parameter combinations approaching the Routh–Hurwitz stability boundaries. As a result, the frequency-response analysis and the analytical criterion consistently demonstrate that instability is more likely to occur close to resonance, especially in circumstances with high excitation and low damping.

6. Bifurcation Analysis

In this section, let's begin by analyzing the bifurcation diagram, the largest Lyapunov exponent LLE, Poincaré maps, and phase portraits of the structure at certain key parameters. This visualization serves as a valuable tool for understanding the transition from order to chaos in nonlinear systems, which involves the emergence of new stable points. On the other hand, LLE examination measures the stability of the dynamical model by exploring solutions nearby it [41]. The bifurcation diagram of the function $z(t)$ with the forcing coefficient f_a and damping coefficient μ_1 are portrayed in Figs. 11(a) and 12(a), Figs. 11(b) and 12(b) display the corresponding LLE, and Figs. 11(c) and (d), and Figs. 12(c) and (d) replicate the phase portraits which are depicted by blue curves and Poincaré maps which are marked by red dots. The simulated figures are derived at various values of the forcing coefficient f_a and damping coefficient μ_1. Initially, under low values of f_a, for instance ($f_a = 0.1$), the system in Fig. 11(a) exhibits a single stable steady-state, which is in accordance with the Poincaré maps given in Fig. 11(c), indicating a highly periodic and stable behavior. Moreover, we noticed through the interval $f_a \in [0, 0.5)$ that LLE of λ is portrayed below the line $\lambda = 0$ which emphasizes that the structure's motion is headed towards periodicity.

The phase portrait shows smooth, looping orbits, confirming the system runs predictably. At this level of excitation, everything remains orderly, making it ideal for tasks that require reliable, repeatable results. As f_a climbs above 0.5, the diagram turns into a messy jumble of points showing signs of chaos and unpredictability. At this range, the LLE of λ got rise above the line $\lambda = 0$ which is evidence for the chaotic motion. Unlike the neat patterns seen when the system is less exciting, the Poincaré map at high levels of excitement (Fig. 11(d)) displays a tangled and scattered spread of points. The phase portrait confirms the presence of chaos, displaying irregular, non-repeating paths. This illustrates how increasing the forcing coefficient transitions the system from a stable to a chaotic state. This kind of behavior is crucial for systems where reliability is key. It highlights the importance of having strategies in place to manage chaos when things become highly chaotic. This is often how chaos starts in complex systems, underscoring the need for careful control.

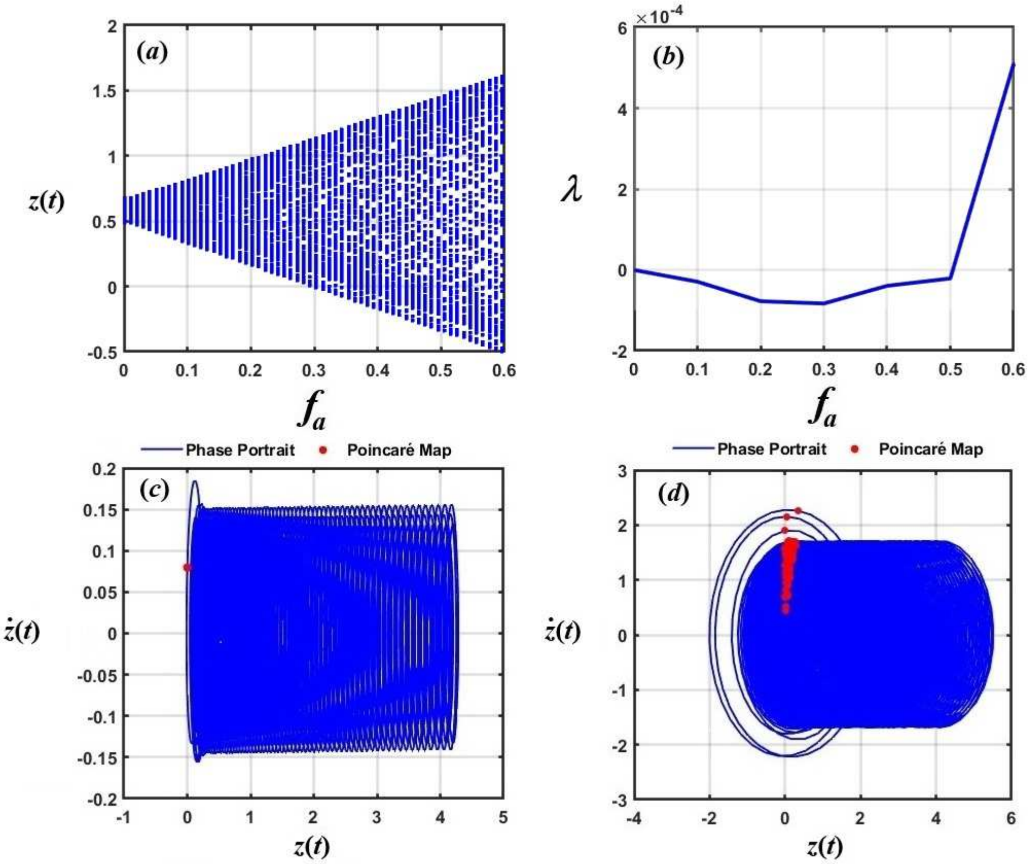

Fig. 11. (a) Bifurcation diagram, with the forcing coefficient f_a, Poincaré maps, and phase portraits of z(t), (b) Corresponding LLE, (c) At $f_a = 0.1$, and (d) At $f_a = 0.55$.

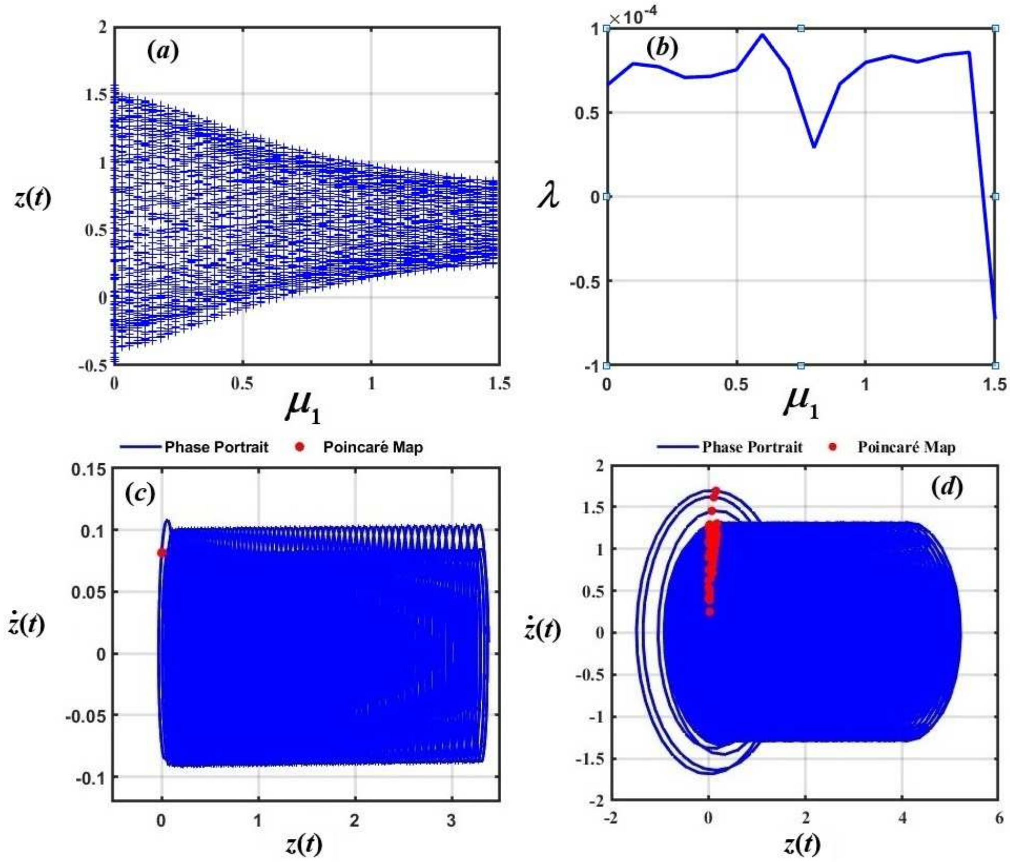

Fig. 12. (a) Bifurcation diagram, with the damping coefficient μ_1, Poincaré maps, and phase portraits of z(t), (b) Corresponding LLE, (c) At $\mu_1 = 1.4$, and (d) At $\mu_1 = 0.3$.

Table 2. Methodological comparison between present study and Vasudevan et al. [24].

Aspect	Vasudevan et al. [24]	Present study
Control strategy	Linear Positive Position Feedback (PPF)	Time-delayed nonlinear integral Positive Position Feedback (TD-NIPPF)
Consideration of time delay	Not applicable	Explicitly modeled and analyzed
Nonlinear integral action	Not applicable	Applicable
Stability analysis	Frequency response, Poincaré maps	Frequency response, Poincaré maps, bifurcation diagrams
Nonlinearity (Chaotic motion)	Not studied	chaotic–periodic transition analysis
Large Lyapunov Exponent LLE	Not applicable	Validated
Vibration reduction efficiency	98.5%	99.2% (no delay), 99.5% (with delay)
Controller reliability	Effective	More reliable under realistic delayed feedback

On the other hand, let's illustrate how structural dynamics evolve with increasing damping factor μ_1. At low values of μ_1, Fig. 12(a) displays a chaotic behavior, characterized by irregular, unpredictable trajectories, indicating complex oscillations and a minimal rate of energy dissipation. By observing the LLE of λ which is above the zero line of λ in the range $\mu_1 \in [0,1.4)$, the motion exhibits a chaotic pattern. Besides, the scattered points in Poincaré map in Fig. 12(d) reveal a chaotic dynamic. As μ_1 increases, the diagram gradually narrows, signifying a suppression of oscillatory dynamics. Eventually, the structure converges to a single, stable amplitude, demonstrating the stabilizing influence of damping. Beyond a certain threshold (approximately $\mu_1 > 1.4$), the system reaches a steady-state regime with minimal fluctuation, indicating overdamped behavior as plotted in Fig. 12(c). This is congruent to Fig. 12(b), in which the LLE of λ is going to be below the zero line of λ. These results show how the system moves from chaotic to more predictable behavior as μ_1 increases, which is something often seen in systems that lose energy over time.

7. Conclusion

A single DOF model representing the fundamental lateral bending mode of the fixed monopile-supported offshore wind turbine tower has been examined as a nonlinear dynamical system, which typically characterizes the dynamic response under environmental conditions, with a TD-NIPPF controller employed to minimize potentially hazardous oscillations. We employed the MSA to obtain approximate solutions up to the second-order approximation. These outputs are confirmed numerically through graphs using the RK-4 approach. The modulation equations and every state of external resonance are identified. The system's two behaviors, periodic and chaotic, are explored using bifurcation diagrams, Poincaré maps, and phase portraits, in addition to the LLE technique, which aligns well with our findings. Additionally, after attaching the TD-NIPPF device to the wind turbine tower, the frequency response curves are illustrated. Furthermore, we have portrayed the parameter impact of the most significant factors on the wind turbine tower to measure how high or low the oscillation amplitude of the model is. Additionally, we conducted a stability analysis at the worst resonance states. Before inserting the TD-NIPPF, the amplitude was 1326.65. After insertion, the amplitude reached 9.56, at which the controller's effectiveness was 99.2%. Moreover, the effect of the time delay was remarkable at $\tau = 0.015$, and the amplitude was mitigated up to 6.756. The effectiveness of TD-NIPPF was enhanced by 99.5%, thereby maximizing the efficiency of the wind turbine structure. Compared with previous works, as shown in Table 2, we have maximized the effectiveness of the considered controller, making it more reliable than the controller applied in [24], and ensuring high performance of the wind turbine. The proposed single DOF model is applicable for preliminary design and global dynamical response estimation of fixed-base offshore wind turbine slender towers, especially when the response is regulated by the fundamental bending mode, under combined wind–wave–seismic excitation, where the excitation energy is closely focused on the fundamental frequency. In addition, the model is effective when the soil conditions are stiff to medium-dense soil profiles. However, the model has limitations, as it does not take into consideration the impact of higher-mode contributions, rotor-nacelle coupling, and soil–structure interaction effects. As a result, it might not be appropriate for situations involving strong nonlinear coupling between environmental loads, local stress examination, and soft foundations. In further studies, we look forward to making our research less theoretical, more practical and experimental, and to employing additional analytical and numerical techniques to accurately analyze these models. In addition, we will attempt to enhance the performance of the controller under consideration.

Author Contributions

T.S. Amer planned the scheme, initiated the project, and contributed to supervision, conceptualization, resources, methodology, formal analysis, validation, visualization, and reviewing; M.K. Abohamer contributed to supervision, resources, methodology, validation, visualization, writing–original draft preparation, and reviewing; T.A. Bahnasy contributed to conceptualization, formal analysis, validation, writing–original draft preparation, and reviewing; I.S. Hamada conducted the software implementation, validation, data curation, methodology, corroboration, writing–original draft preparation, rereading, and editing; A.M. Farag contributed to supervision, formal analysis, visualization, and reviewing. The manuscript was written through the contribution of all authors. All authors discussed the results, reviewed, and approved the final version of the manuscript.

Acknowledgments

Not applicable.

Conflict of Interest

The authors declared no potential conflicts of interest concerning the research, authorship, and publication of this article.

Funding

The authors received no financial support for the research, authorship, and publication of this article.

Data Availability Statements

The datasets generated and/or analyzed during the current study are available from the corresponding author on reasonable request.

Nomenclature

TD-NIPPF	Time-delayed nonlinear integral positive position feedback
GE	Governing equation
MSA	Multiple-scales approach
RK-4	4th-order Runge-Kutta method
LLE	Largest Lyapunov exponent
NVF	Negative velocity feedback
PD	Proportional derivative
NSC	Nonlinear saturation control
TMDs	Tuned mass dampers

References

[1] Agbayani, N., Vega, R., The rapid evolution of wind turbine tower structural systems: A historical and technical overview, *Structures Congress*, 2012, 1201-1212.
[2] Damiani, R.R., Design of offshore wind turbine towers, Offshore Wind Farms: Technologies, Design and Operation, *Woodhead Publishing*, 2016, 263-357.
[3] Van der Woude, C., Narasimhan, S., A study on vibration isolation for wind turbine structures, *Engineering Structures,* 60, 2014, 223–234.
[4] Dagli, Z.B.Y., Tuskan, Y., Gokkus, U., Evaluation of offshore wind turbine tower dynamics with numerical analysis, *Advances in Civil Engineering,* 2018, 3054851.
[5] Wu, X., Hu, Y., Li, Y., Yang, J., Duan, L., Wang, T., Adcock, T., Jiang, Z., Gao, Z. Lin, Z., Borthwick, A., Liao, S., Foundations of offshore wind turbines: A review, *Renewable and Sustainable Energy Reviews,* 104, 2019, 379-393.
[6] Fang, Z. W., Zhang, Li, X., Ding, H., Chen, L. Q., Considerations for the structural analysis and design of wind turbine towers: A review, *Renewable and Sustainable Energy Reviews*, 137, 2021, 110447.
[7] Liu, X., Lu, C., Li, G., Godbole, A., Chen, Y., Tower load analysis of offshore wind turbines and the effects of aerodynamic damping, *Energy Procedia*, 105, 2017, 373-378.
[8] Fitzgerald, B., Sarkar, S., Staino, A., Improved reliability of wind turbine towers with active tuned mass dampers (ATMDs), *Journal of Sound and Vibration* 419, 2018, 103-122.
[9] Peng, J., Xiang, M., Wang, L., Xie, X., Sun, H., Yu, J., Nonlinear primary resonance in vibration control of cable-stayed beam with time delay feedback, *Mechanical Systems and Signal Processing*, 137, 2020, 106488.
[10] Hamed, Y.S., Aly, A.A., Saleh, B., Alogla, A.F., Aljuaid, A.M., Alharthi, M.M., Vibration performance, stability and energy transfer of wind turbine tower via PD controller, *Computers, Materials & Continua*, 64(2), 2020, 871-886.
[11] Hamed, Y.S., Aly, A.A., Saleh, B., Alogla, A.F., Aljuaid, A.M., Alharthi, M.M., Nonlinear structural control analysis of an offshore wind turbine tower system, *Processes*, 8(1), 2020, 1-15.
[12] Abualnaja, K.M., Amer, Y.A., El-Sayed, A.T., Ahmed, E., Hamed, Y.S., Response analysis and controlling the nonlinear vibration of Van Der-Pol duffing oscillator connected to the NIPPF controller, *IEEE Access*, 9, 2021, 91836-91849.
[13] Nayfeh, A.H., *Perturbation methods*, Wiley-VCH Verlag GmbH and Co. KGaA, Weinheim, 2004.
[14] Lackner, M.A., Rotea, M.A., Passive structural control of offshore wind turbines, *Wind Energy*, 14(3), 2011, 373–388.
[15] Awada, A., Younes, R., Ilinca, A., Review of vibration control methods for wind turbines, *Energies*, 14, 2021, 3058.
[16] Kandil, A., El-Ganaini, W.A., Investigation of the time delay effect on the control of rotating blade vibrations, *European Journal of Mechanics-A/Solids,* 72, 2018, 16-40.
[17] Amer, Y.A., Bahnasy, T.A., Duffing oscillator's vibration control under resonance with a negative velocity feedback control and time delay, *Sound & Vibration*, 55(3), 2021, 191-201.
[18] Hamed, Y.S., Kandil, A., Influence of time delay on controlling the nonlinear oscillations of a rotating blade, *Symmetry*, 13, 2021, 85.
[19] Lackner, M.A., Rotea, M.A., Passive structural control of offshore wind turbines, *Wind Energy*, 14(3), 2011, 373-388.
[20] Guimarães, P.V.B., Morais, M.V.G., Avila, S.M., Tuned mass damper inverted pendulum to reduce offshore wind turbine vibrations, *Vibration Engineering and Technology of Machinery, Mechanisms and Machine Science*, 23, 2015, 379-388.
[21] Brodersen, M.L., Bjørke, A.S., Høgsberg, J., Active tuned mass damper for damping of offshore wind turbine vibrations, *Wind Energy*, 20, 2017, 783-796.
[22] Ghassempour, M., Failla, G., Arena, F., Vibration mitigation in offshore wind turbines viatuned mass damper, *Engineering Structures*, 183, 2019, 610-636.
[23] Li, J., Wang, G., Li, Z., Yang, S., Chong, W.T., Xiang, X., A review on development of offshore wind energy conversion system, *International Journal of Energy Research*, 44(12), 2020, 9283-9297.
[24] Vasudevan, S., Kondayampalayam, V.M., Murugesan, A., Recent developments in offshore wind energy systems: Technologies and practices, *International Journal of Advances in Applied Sciences*, 11(3), 2022, 220 -231.
[25] Alsaadi, A., Hamed, Y.S., On controlling, vibration performance and energy transfer of an offshore wind turbine tower system via PPF controller, *European Journal of Pure and Applied Mathematics*, 16(4), 2023, 2703-2728.
[26] Elias, S., Beer, M., Vibration control and energy harvesting of offshore wind turbines installed with TMDI under dynamical loading, *Engineering Structures*, 315, 2024, 118459.
[27] Yan, S., Wang, Y., Pang, F., Zhang, W., Zhang, B.-L., Wind and wave-induced vibration reduction control for floating offshore wind turbine using delayed signals, *Journal of Marine Science and Engineering*, 12, 2024, 1113.
[28] Yang, Y., Liang, F., Zhu, Q., Zhang, H., An overview on structural health monitoring and fault diagnosis of offshore wind turbine support structures, *Journal of Marine Science and Engineering*, 12, 2024, 377.
[29] Amer, Y.A., El-Sayed, A.T., Agwa, M.M., Controlling wind turbine tower vibration under external force by applying control systems combination, *Scientific Reports*, 14, 2024, 18597.
[30] Afridi, S.K., Koondhar, M.A., Jamali, M.I., Alaas, Z.M., Alsharif, M.H., Kim, M., Winds of Progress: An in-depth exploration of offshore, floating, and onshore wind turbines as cornerstones for sustainable energy generation and environmental stewardship, *IEEE Access*, 12, 2024, 66147-66166.
[31] Amer, T.S., Ismail, A.I., Amer, W.S., Evaluation of the stability of a two degrees-of-freedom dynamical system, *Journal of Low Frequency Noise, Vibration and Active Control,* 42(4), 2023, 1578-1595.
[32] Amer, T.S., Moatimid, G.M., Zakria, S.K., Galal, A.A., Vibrational and stability analysis of planar double pendulum dynamics near resonance, *Nonlinear Dynamics*, 112, 2024, 21667-21699.
[33] El-Sabaa, F.M., Amer, T.S., Gad, H.M., Bek, M.A., On the motion of a damped rigid body near resonances under the influence of harmonically external force and moments, *Results in Physics*, 19, 2020, 103352.
[34] Amer, W.S., Amer, T.S., Starosta, R., Bek, M.A., Resonance in the cart-pendulum system-an asymptotic approach, *Applied Sciences*, 11(23), 2021, 11567.
[35] Elneklawy, A.H., Amer, T.S., Elkilany, S.A., Abo Seliem, A.S., Hegazy, N., Damping-Based Attitude Control of a Gyrostatic Satellite in Resistive Media, *Journal of Applied and Computational Mechanics*, 2025. DOI: 10.22055/jacm.2025.48699.5434

[36] Amer, T.S., Abdelhfeez, S.A., Elbaz, R.F., Abohamer, M.K., Investigation of the dynamical analysis, stability, and bifurcation for a connected damped oscillator with a piezoelectric harvester, *Journal of Vibration Engineering and Technologies*, 13, 2025, 155.
[37] Strogatz, S.H., *Nonlinear dynamics and chaos: With applications to physics, biology, chemistry, and engineering*, second edition, Princeton University Press, Princeton, NJ, USA, 2015.
[38] Bauomy, H.S., EL-Sayed, A.T., Amer, T.S., Abohamer, M.K., Negative derivative feedback control and bifurcation in a two-degree-of-freedom coupled dynamical system, *Chaos, Solitons and Fractals,* 193, 2025, 116138.
[39] Abohamer, M.K., Amer, T.S., Abdelhfeez, S.A., Eldawoody, D.A., Elbaz, R.F., Vibration analysis, stability assessment, and chaotic behavior of a damped oscillator coupled with a spherical pendulum and a piezoelectric transducer, *Nonlinear Dynamics*, 113, 2025, 24343-24381.
[40] Bahnasy, T.A., Amer, T.S., Elameer, A.S., Abohamer, M.K., Chaotic behavior analysis of a hanging wire system with NIPPFC controller, *Journal of Low Frequency Noise, Vibration and Active Control*, 2025, 1-23.
[41] Alluhydan, K., Amer, Y.A., EL-Sayed, A.T., EL-Sayed, M.A., The Impact of the Nonlinear Integral Positive Position Feedback (NIPPF) Controller on the Forced and Self-Excited Nonlinear Beam Flutter Phenomenon, *Symmetry*, 16(9), 2024, 1143.
[42] Schiller, S., Perchtold, D., Steiner, W., Nonlinear and chaotic dynamics of a vibratory conveying system, *Nonlinear Dynamics*, 111, 2023, 9799-9814.
[43] Nayfeh, A.H., Balachandran, B., *Applied nonlinear dynamics: analytical, computational, and experimental methods*, Wiley-VCH Verlag GmbH and Co. KGaA, Weinheim, 2008.
[44] Arany, L., Bhattacharya, S., Macdonald, J., Hogan, J., Design of monopiles for offshore wind turbines in 10 steps, *Soil Dynamics and Earthquake Engineering*, 92, 2017, 126–152.

Appendix

The factors γ_{ij} $(i, j = 1,\ldots,4)$ of the Jacobian matrix J provided in Eq. (17) are:

$$\begin{aligned}
&\gamma_{11} = -\frac{\mu_1}{2}, \quad \gamma_{12} = -\frac{f_a}{2\omega_1}\sin\theta_{10}, \quad \gamma_{13} = \frac{\beta_1}{2\omega_1}\sin(\theta_{20}-\omega_2\tau), \quad \gamma_{14} = \frac{\beta_1 b_{10}}{2\omega_1}\cos(\theta_{20}-\omega_2\tau)\\
&\gamma_{21} = -\frac{\beta_1 b_{10}}{2\omega_1 a_{10}^2}\cos(\theta_{20}-\omega_2\tau) + \frac{f_a}{2\omega_1 a_{10}^2}\sin\theta_{10}, \quad \gamma_{22} = -\frac{f_a}{2\omega_1 a_{10}}\cos\theta_{10},\\
&\gamma_{23} = \frac{\beta_1}{2\omega_1 a_{10}}\cos(\theta_{20}-\omega_2\tau), \quad \gamma_{24} = -\frac{\beta_1 b_{10}}{2\omega_1 a_{10}}\sin(\theta_{20}-\omega_2\tau)\\
&\gamma_{31} = -\frac{\beta_3}{2\omega_2}\sin(\theta_{20}+\omega_1\tau), \quad \gamma_{32} = 0, \quad \gamma_{33} = -\frac{\mu_2}{2}, \quad \gamma_{34} = -\frac{\beta_3 a_{10}}{2\omega_2}\cos(\theta_{20}+\omega_1\tau)\\
&\gamma_{41} = -\frac{\beta_1 b_{10}}{2\omega_1 a_{10}^2}\cos(\theta_{20}-\omega_2\tau) - \frac{\beta_3}{2\omega_2 b_{10}}\cos(\theta_{20}+\omega_1\tau) + \frac{f_a}{2\omega_1 a_{10}^2}\sin\theta_{10},\\
&\gamma_{42} = -\frac{f_a}{2\omega_1 a_{10}}\cos\theta_{10}, \quad \gamma_{43} = \frac{\beta_1}{2\omega_1 a_{10}}\cos(\theta_{20}-\omega_2\tau) + \frac{\beta_3 a_{10}}{2\omega_2 b_{10}^2}\cos(\theta_{20}+\omega_1\tau),\\
&\gamma_{44} = -\frac{\beta_1 b_{10}}{2\omega_1 a_{10}}\sin(\theta_{20}-\omega_2\tau) + \frac{\beta_3 a_{10}}{2\omega_2 b_{10}}\sin(\theta_{20}+\omega_1\tau).
\end{aligned} \tag{A.1}$$

In addition, the coefficients Γ_r $(r = 1, 2, 3, 4)$ of Eq. (18) are:

$$\begin{aligned}
&\Gamma_1 = -\sum_{i=1}^{4}\gamma_{ii}\\
&\Gamma_2 = \frac{1}{2!}\sum_{i=1}^{4}\sum_{j=1}^{4}\gamma_{ii}\gamma_{jj} - \gamma_{ij}\gamma_{ji}\\
&\Gamma_3 = -\frac{1}{3!}\sum_{i=1}^{4}\sum_{j=1}^{4}\sum_{k=1}^{4}\gamma_{ii}\gamma_{jj}\gamma_{kk} - 3\gamma_{ii}\gamma_{jk}\gamma_{kj} + 2\gamma_{ij}\gamma_{jk}\gamma_{ki}\\
&\Gamma_4 = \frac{1}{4!}\sum_{i=1}^{4}\sum_{j=1}^{4}\sum_{k=1}^{4}\sum_{l=1}^{4}\gamma_{ii}\gamma_{jj}\gamma_{kk}\gamma_{ll} - 6\gamma_{ii}\gamma_{jj}\gamma_{kl}\gamma_{lk} + 8\gamma_{ii}\gamma_{jk}\gamma_{kl}\gamma_{lj} + 3\gamma_{ij}\gamma_{ji}\gamma_{kl}\gamma_{lk} - 6\gamma_{ij}\gamma_{jk}\gamma_{kl}\gamma_{li}
\end{aligned} \tag{A.2}$$

ORCID iD

T.S. Amer https://orcid.org/0000-0002-6293-711X
M.K. Abohamer https://orcid.org/0000-0001-8679-0565

How to cite this article: Amer T.S., Abohamer M.K., Bahnasy T.A., Hamada I.S., Farag A.M. Vibration and Energy Optimization in Offshore Wind Towers via Time-Delayed Nonlinear Integral Positive Position Feedback Control, *J. Appl. Comput. Mech.*, xx(x), 2026, 1–15. https://doi.org/10.22055/jacm.2026.48900.5585